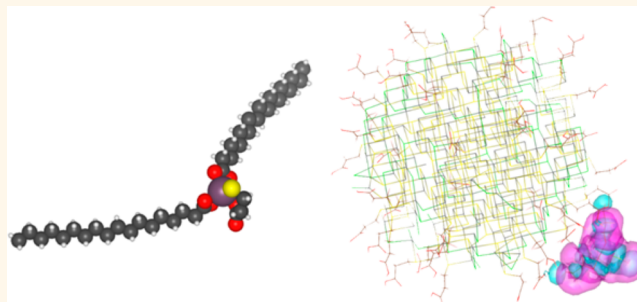# Electronically Active Impurities in Colloidal Quantum Dot Solids

Graham H. Carey,[†,§] Illan J. Kramer,[†,§] Pongsakorn Kanjanaboos,[†] Gabriel Moreno-Bautista,[†] Oleksandr Voznyy,[†] Lisa Rollny,[†] Joel A. Tang,[‡] Sjoerd Hoogland,[†] and Edward H. Sargent*,[†]

[†]The Edward S. Rogers Department of Electrical and Computer Engineering, University of Toronto, 10 King's College Road, Toronto, Ontario M5S 3G4, Canada and [‡]Department of Chemistry, University of Toronto, 80 St. George Street, Toronto, Ontario M6S 3H6, Canada. [§]These authors contributed equally.

ABSTRACT Colloidal quantum dot films have seen rapid progress as active materials in photodetection, light emission, and photovoltaics. Their processing from the solution phase makes them an attractive option for these applications due to the expected cost reductions associated with liquid-phase material deposition. Colloidally stable nanoparticles capped using long, insulating aliphatic ligands are used to form semiconducting, insoluble films *via* a solid-state ligand exchange in which the original ligands are replaced with short bifunctional ligands. Here we show that this ligand exchange can have unintended and undesired side effects: a high molecular weight complex can form, containing both lead oleate and the shorter conductive ligand, and this poorly soluble complex can end up embedded within the colloidal quantum dot (CQD) active layer. We further show that, by adding an acidic treatment during film processing, we can break up and wash away these complexes, producing a higher quality CQD solid. The improved material leads to photovoltaic devices with reduced series resistance and enhanced fill factor relative to controls employing previously reported CQD solids.

KEYWORDS: colloidal quantum dot · photovoltaics · complex · impurities · ligands · electroluminescence

Colloidal quantum dots (CQDs) are an attractive option for low-cost, high-efficiency optoelectronic applications such as light-emitting devices,[1,2] photodetectors,[3] and solar cells.[4,5] CQDs are solution-processed nanoparticles (typically semiconductor materials such as PbS, PbSe, CdS, *etc*.) which, through quantum size effect tuning, enable a broad range of bandgaps compared to the compositionally determined bandgap of the constituent bulk material.[6] This characteristic is particularly useful for photovoltaic applications since it allows even a single materials system to become spectrally versatile.[7−9]

CQD photovoltaic device performance has progressed quickly in the past decade of research: certified power conversion efficiencies have reached 8.55% in recent reports.[10] Recent studies have begun to address CQD device properties beyond instantaneous power conversion efficiency, looking, for example, at manufacturability.[11,12] A key metric for manufacturability is the reproducibility of performance: consistency from device to device, substrate to substrate, and CQD synthesis batch to batch. A statistically repeatable process is an important ingredient in achieving a scalable end product.

The method of CQD film deposition influences device performance and repeatability. Recent reports have revealed notable differences between the standard spin-coated layer-by-layer film formation technique and a more controlled spray-coating deposition method, the latter employing near-monolayer control of CQD buildup and termed sprayLD.[13,14]

In the present work, we investigate the origins of performance variability in CQD photovoltaic device performance based on legacy layer-by-layer methods; and we then develop a chemical method that overcomes this variability. The method is applicable to films formed using a wide suite of deposition methods.

RESULTS AND DISCUSSION

We began with analytical studies of the composition of high-performing films, seeking possible correlations between materials composition and performance. Solid-state
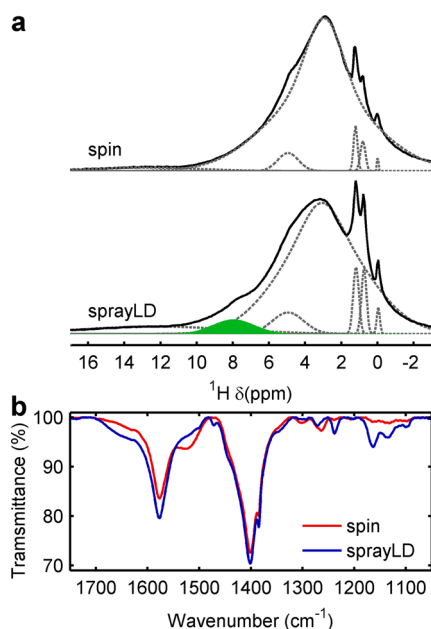
Figure 1. (a) Proton solid-state NMR measurements of our typical (spin, top) films and of our films exhibiting a tighter photovoltaic performance distribution (sprayLD, bottom) (solid lines). Peak fits indicating phoshponic acid (~12 ppm), the MPA carbon chain (~0−2 ppm), and residual methanol and water (~3 ppm and ~5 ppm, respectively) are represented by dashed lines. The presence of a protonated carboxylic acid is observed in the sprayLD case at ~8 ppm (highlighted in green). (b) FTIR spectroscopy of the same films as (a). The acid peak shifts toward a deprotonated carboxylate (shoulder at ~1500−1550 cm^{-1}) in the spin case, whereas the increase at 1600−1700 cm^{-1} for sprayLD indicates the enhanced presence of carboxylic acid.

nuclear magnetic resonance (SS NMR) (Figure 1a) revealed that the signal associated with the presence of COOH groups, potentially associated with protonated 3-mercaptopropionic acid (MPA) used in cross-linking, was present at a higher concentration in the better performing films produced using the sprayLD method.[13,14] Similarly, Fourier transform infrared spectroscopy (FTIR) studies showed a marked difference between bound and unbound carboxylate signals (Figure 1b) with the higher variability spin coating procedure showing greater evidence of a bound (and thus deprotonated) COO− group (1500−1550 cm^{-1} range).[15]

In each case, the films in question had been fabricated by depositing oleic acid-capped PbS CQDs and exchanging surface ligands with a shorter bifunctional molecule, MPA. The film was then rinsed with methanol to remove any unbound MPA and oleic acid. Since both the initial and final ligands include a carboxylic acid functional group, the NMR and FTIR results are not conclusive as to the origins of the COOH and COO− in the final films. Both oleic acid and MPA are highly soluble in methanol, therefore shifting the focus onto possible low-solubility complexes.

We turned to density functional theory (DFT) to investigate several potential complexes and how they would influence the density of states if incorporated into CQD films. Parts a−d of Figure 2 compare the predicted effect of MPA, deprotonated MPA, lead oleate, and a lead oleate−MPA complex on density of states. Oleic acid alone was not considered as it does not result in a luminescent long wavelength state in PbS CQD films.[16] MPA, whether protonated or not, is not predicted to produce midgap states. The same applies to lead oleate. However, the introduction of lead oleate with a lead-bound MPA molecule near the dot surface is predicted to produce an electronic trap state in the bandgap localized on the molecular complex (Figure 2d). The origin of lead oleate on the surface of the film comes from the solid state exchange procedure itself. It has been shown to desorb in abundance from PbS CQD surfaces during solid state ligand exchange in addition to the oleic acid ligand alone.[17] The blue shift that could be expected due to slight CQD shrinkage is not observed. We propose that, in highly coupled CQD films, this process competes with mild CQD aggregation that accounts for the net (though small) red shift.[18] All DFT calculations were undertaken using charge-balanced PbS CQDs whose surfaces are therefore trap-free. It has been previously shown that unbalanced CQDs contain primarily shallow trap states on the surface[19] distinct from the relatively deep traps localized off the surface and on the nearby complex for the case of the complex-associated traps of Figure 2.

To gain experimental insight into the identity and energetics of possible electronic trap states associated with complexes, we investigated the origins of midgap luminescence observed in the higher variability spin-coated films. In light of the DFT results, we synthesized lead oleate−MPA in bulk and studied the photoluminescence spectra of the resulting waxy solid, comparing these spectra with those of pure lead oleate (Figure 2e). While pure lead oleate shows no measurable signal in the observed range, the lead oleate−MPA complex produces a sizable signal near 1550 nm.

We sought to verify whether this low energy luminescence would persist if the complex were incorporated into CQD films at realistically low concentrations. We added a small volume of excess lead oleate during the deposition of a spray-coated film (which consistently show no measurable light emissions signal beyond their 1150 nm band-edge luminescence before excess lead oleate addition). The resultant film was analyzed by electroluminescence (Figure 2f) and was found to exhibit a strong 1550 nm luminescent feature. As seen in DFT, defects on the CQD surface are predicted to result in one charge carrier localized on the defect site and one delocalized over the QD. The overlap between these two carriers is small, and the defect appears dark in the predicted absorption spectrum, as well as weak predicted luminescence. Also from DFT, the defect due to the complex localizes both
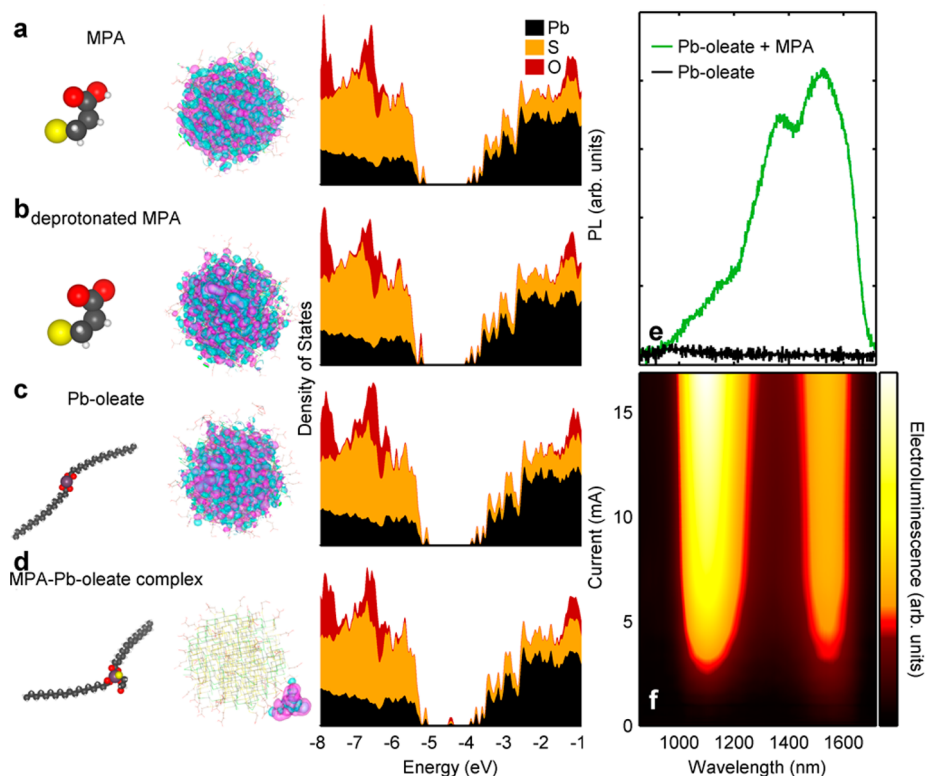
Figure 2. DFT wave function calculations of an MPA-terminated PbS CQDs (a), deprotonated MPA terminated PbS CQDs (b), and MPA terminated PbS CQD with (c) lead oleate or (d) a lead oleate−MPA complex near the CQD surface. The wave function within the CQD shifts entirely to the complex in (d) but remains in the core of the CQD in cases (a−c), indicating the presence of a midgap electronic state. The accompanying density of states calculations by DFT illustrate the emergence of a midgap state for the lead oleate−MPA complex case. (e) Photoluminescence of lead oleate treated with methanol (black curve) and dilute MPA (green curve) rinses showing the ∼1550 nm luminescence of the lead oleate−MPA complex. (f) A sprayLD film with an excess of lead oleate added to the CQD solution illustrates the reemergence of the long wavelength peak as a lead oleate−MPA complex forms.

electrons and holes onto the complex, leading to a strong carrier overlap and thus a bright luminescent state. Both single-molecule (Figure 2d) and polymerized complexes (Figure S1, Supporting Information) were modeled and exhibited the same localized state on the molecule with similar midgap defects.

Thus, from a combination of DFT, the synthesis of the posited low energy complex, its photoluminescence as a pure material, and its persistent luminescence when incorporated into CQD films, we had gathered a body of evidence that a lead oleate−MPA complex could lead to performance-limiting midgap electronic states.

We sought a chemical means of removing such a complex from CQD films to ensure reproducibility across all fabrication methods. We began by testing the solubility of the synthesized lead oleate−MPA complex in a variety of standard polar and nonpolar solvents (Figure 3a−e: water, methanol, acetonitrile, octane, and toluene, respectively). Unfortunately, the complex proved completely insoluble in each case. This further strengthened the supposition that, once generated during solid-state ligand exchange, such a complex would likely remain incorporated into films and offer the potential to degrade performance as an impurity-based recombination center.

Considering that neither polar nor nonpolar solvents appeared to affect the complex solubility, a deeper structural examination of the complex itself was required. While standard characterization techniques were precluded due to the complete insolubility of the complex and the complicating inclusion of heavy lead atoms, we obtained hints about structure by synthesizing related complexes. Mixing lead oleate with 1,2 ethanedithiol (EDT), the other major bifunctional ligand commonly employed in PbS CQD films,[20] led to the formation of a similar waxy solid (Figure S2, Supporting Information). By contrast, mixing lead oleate with ligands with single lead-binding functional groups (thioglycerol, for example) did not produce any trace of a solid complex. These results suggest that the combination of lead oleate and a bifunctional molecule may create a complex of linked lead oleate moieties and an overall large, insoluble compound. Additionally, we posit that formation of impurity complexes in CQD solid formation may be relatively widespread wherever bifunctional ligands are employed.

A large molecular weight complex is consistent with the difficulty in dissolving it using the solvents of Figure 3a−e. We posited that it would be necessary to cleave the linkages at the MPA-bound lead centers
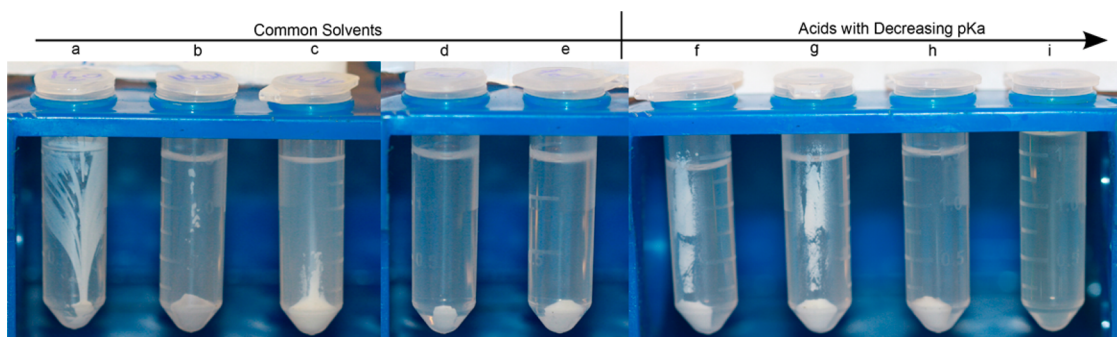
Figure 3. Solubility of the lead oleate—MPA complex in common solvents including (a) water, (b) methanol, (c) acetonitrile, (d) octane, and (e) toluene. Solubility of the same lead oleate—MPA complex in acids with decreasing pK_a including (f) acetic acid, (g) lactic acid, (h) formic acid, and (i) pyruvic acid.

and that this could be accomplished by reprotonating the carboxylate MPA functional group. This could allow individual lead oleate—MPA moieties to dissolve in a common solvent such as methanol. Parts f—i of Figure 3 show a suite of acids, pictured in order of decreasing pK_a (acetic, lactic, formic, and pyruvic, respectively), at roughly 0.7 M in methanol. While the first three fail to fully dissolve the complex, pyruvic acid in methanol readily dissolves the entire added aliquot of the complex.

We therefore explored the addition of a low concentration of pyruvic acid to the methanol rinse step that is implemented immediately after the solid-state ligand exchange, with the goal of breaking up, dissolving, and washing away the embedded lead oleate—MPA complex. We employed a range of pyruvic acid concentrations from 0 to 0.8% v/v in methanol for this complex-rinse processing step. We investigated both device performance and electroluminescence spectra (Figure 4a, increasing pyruvic concentration top to bottom). The control devices exhibited a significant feature at 1500 nm. This feature disappeared when pyruvic acid was added to the methanol rinse. FTIR (Figure 4b) revealed that eliminating the complex shifted the carboxylate stretch from the bound signature (COO— dominated, 1500–1550 cm^{-1}) to the unbound (protonated carboxylate, 1600–1700 cm^{-1}). There was no significant change in the absorption spectra of the films with and without pyruvic acid treatment (Figure S3, Supporting Information).

We investigated the impact of the new complex-removal step on solar cell performance. Exploring the same range of pyruvic acid concentrations as previously outlined, we found that power conversion efficiency was maximized when films were treated using 0.2% v/v pyruvic acid in methanol (Figure S4, Supporting Information); beyond 0.8% v/v treatment, device performance was significantly lower due to decreasing open-circuit voltage (V_{OC}) without any further corresponding fill factor (FF) gain. In the subsequently fabricated films, the series resistance (R_S) and the fill factor vary widely in the control devices

(Figure 4c, red). We propose that uncontrolled variations in available lead oleate (due to synthesis variations, post-synthesis washing procedures, and solid-state exchange conditions) account for sample-to-sample variability. By contrast, removing the complex with pyruvic acid treatment (Figure 4c, blue) leads to consistently lower R_S and higher FF, even using the same dot batches with their presumed variations in initial oleic acid/lead oleate concentrations. This trend holds true when compared with a large control sample set and many initial CQD batches (Figure 4c) as well as when considering only side-by-side controls (Figure S5, Supporting Information). For all histograms, each data point represents a device on a distinct substrate. The new treatment thus allows the fabrication of more consistently conductive films. Typical head-to-head photovoltaic performance with and without pyruvic acid treatment is shown in Figure S6 (Supporting Information), and full statistical figures of merit for devices in Figure 4c are given in Table S1 (Supporting Information). We propose that the complex, which includes high molecular weight fatty acid complexes, adds series resistance and hampers charge transport at maximum-power-point conditions.

We did observe that it is possible to overtreat the films using higher pyruvic acid concentrations, thereby reducing performance. We offer the following explanation for the formation of electronic defects upon overly aggressively treatment with pyruvic acid. The MPA molecule likely exists in multiple configurations within the film:

(1) surface bound to a CQD solely at the thiol end, with a dangling, protonated carboxylic acid group
(2) bound in a bidentate fashion with both the thiol end and carboxylate end bound to Pb on the surface of a CQD
(3) within the proposed complex wherein both the thiol and carboxylate ends are bound to lead oleate

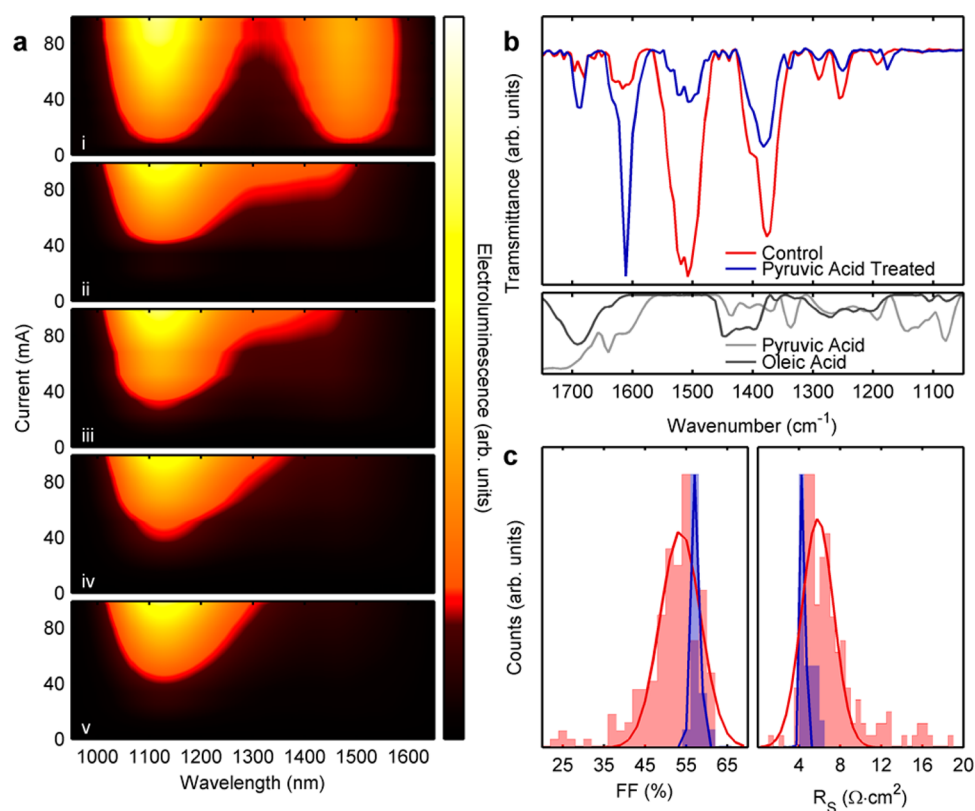We propose that the desired low concentrations of pyruvic acid were sufficient to reprotonate and cleave the

Figure 4. (a) Electroluminescence of CQD solar cell devices with treatments of (i) 0.0% pyruvic acid, (ii) 0.2% pyruvic acid, (iii) 0.4% pyruvic acid, (iv) 0.6% pyruvic acid, and (v) 0.8% pyruvic acid illustrating the removal of the luminescent midgap defect state caused by the lead oleate−MPA complex. (b, top) FTIR transmission of control (untreated film) and pyruvic acid treated film showing the same reduction in relative contribution of a deprotonated carboxylate versus carboxylic acid observed in Figure 1b. (b, bottom) FTIR transmission of pure pyruvic acid and pure oleic acid highlight that the relative peaks are not dominated by free acid introduced within the film. The strong peak at 1700 cm^{-1} for both acids is muted relative to the stronger carboxylate and carboxylic acid peaks found within the films. (c) Histograms of control (red) and pyruvic acid treated devices (blue) with accompanying Gaussian fits illustrating the much tighter distribution with a shifted center toward higher fill factor (left) and lower series resistance (right).

complexes, leading to improved performance and consistency. Higher pyruvic acid concentrations may have brought protons to the surface-bound carboxylates of configuration 2, reprotonating the carboxylate and generating configuration 1. This reaction would leave behind a newly unpassivated surface site on the CQD: a trap.

CONCLUSIONS

This work points to an example of an inorganic−organic complex that can form when surface-bound lead oleate and cross-linking ligands such as MPA and EDT are introduced during CQD film formation. The use of a sufficiently strong acid to reprotonate and cleave the complex prior to its irreversible incorporation in the film leads to its substantial removal and an improvement in performance consistency. The new strategy led to higher device reproducibility by ensuring that electronic transport through the film is dictated by the quantum dots themselves and not by uncontrolled levels of embedded insulating moieties. More broadly, the work suggests that further avenues should be explored that could circumvent complex formation in the first place. Ongoing work on solution-phase exchanges[21] to final capping ligands offers promise in avoiding incorporating undesired impurities at the time of film formation.

METHODS

Lead Oleate−X Synthesis. Lead oleate was prepared by mixing lead oxide with oleic acid at elevated temperature (100 °C for 8 h). Lead oleate was then warmed with a heat gun to ensure full liquid state before being mixed with equal parts of a 10% solution of a bifunctional short ligand (3-mercaptopropionic acid or ethanedithiol) in methanol. The solution was mixed vigorously and centrifuged to separate the resulting precipitate, which was then dried under vacuum for 30 min to remove excess solvent.

Colloidal Quantum Dot Synthesis. PbS quantum dots were synthesized according to a previously published method[22] using a previously reported in-synthesis halide treatment.[5]

Photovoltaic Device Fabrication. CQD films were prepared on TiO$_2$ electrodes (50 nm of TiO$_2$ sputtered on fluorine-doped tin oxide (FTO)-coated glass) using layer-by-layer spin-coating deposition under ambient conditions, depositing a 50 mg mL^{-1} solution of quantum dots in octane at 2500 rpm to obtain layers of roughly 30 nm thickness. Each layer was treated with 1%

3-mercaptopropionic acid in methanol (v/v) and rinsed with either pure methanol (control devices) or a solution of pyruvic acid in methanol (from 0.2 to 1.5% v/v), followed by a final pure methanol rinse and spinning at 2500 rpm after each rinse. Top electrodes were deposited by thermal and electron beam evaporation and consisted of 40 nm of MoO_3, 50 nm of gold, and 150 nm of silver, deposited at a rate of 0.2 (thermal MoO3), 0.4 (electron beam Au), and 1 (thermal Ag) Å/s, at a pressure of $<1 \times 10-6$ mbar.

Photovoltaic Performance Characterization. Current—voltage data were measured with the device at ambient temperature in a constantly purged nitrogen environment, using a Keithley 2400 source meter. The solar spectrum at AM1.5 was simulated to within class A specifications (less than 25% spectral mismatch) with a xenon lamp and filters (ScienceTech; measured intensity of 100 mW cm^{-2}). The source intensity was measured with a Melles—Griot broadband power meter through a circular 0.049 cm^2 aperture. The same aperture was used in device measurements; the aperture is slightly smaller than the top device electrode to avoid overestimating photocurrent. The entire photon fluence passing through the aperture was counted as incident on the device for all current analyses.[23] The spectral mismatch of the system was characterized using a calibrated reference solar cell (Newport). The total AM 1.5 spectral mismatch—taking into account the simulator spectrum and the spectral responsivities of the test cell, reference cell, and broadband power meter—was remeasured periodically and found to be ca. 8.2%. This multiplicative factor, $M = 0.918$, was applied to the current density values of the J—V curve to most closely resemble true AM 1.5 performance.[24]

Luminescence Measurements. Electroluminescence measurements were carried out by connecting a Keithley 2410 source meter to our devices and applying a range of forward bias voltages while reading the resultant current. The luminescence was collected through a set of lenses focused on an optical fiber and connected to an Ocean Optics NIR-512 spectrophotometer. Photoluminescence measurements cofocused the input to the same signal collection optics with a 630 nm wavelength continuous wave laser.

Solid-State NMR. All solid-state NMR experiments were performed on an Agilent DD2 700 MHz spectrometer with a 1.6 mm T2 NB HX Balun probe. Magic angle spinning experiments were conducted while spinning the sample at 25 kHz to ensure that there were no spinning sidebands in the region of interest. 1H chemical shifts were referenced to trimethyl silane ($\delta_{iso} = 0$ ppm) using adamantane as a secondary reference (1H: 1.85 ppm for the high-frequency resonance). For NMR analysis, the curves were fit by a superposition of Gaussians with peak centers corresponding to constituent ligands (MPA $\approx$ 0—2 ppm), residual methanol ($\sim$3 ppm) and water ($\sim$5 ppm) and by a residual synthesis precursor, tetradecyl phosphonic acid ($\sim$12 ppm). The additional $\sim$8 ppm peak was assigned to a protonated carboxylic acid.

Fourier Transform Infrared Spectroscopy. FTIR was performed on a Bruker Tensor spectrometer in transmission mode. Analysis of CQD films was performed by fabricating films as outlined above on glass substrates, manually scraping material off the substrate and mixing the resultant powder with KBr powder in roughly a 1:100 w/w ratio. The mixture was compressed into a thin pellet using a PIKE Technologies pellet press. Reference measurements for pyruvic and oleic acids were carried out by depositing and spreading a small volume of each compound on a KBr disk and immediately measuring. A background subtraction against air was carried out for the entire data set.

Density Functional Theory Calculations. Calculations were carried out using the Quickstep module of the CP2K program suite[25,26] utilizing a dual basis of localized Gaussians and plane waves. The plane wave cutoff was 300 Ry, appropriate for the Goedecker—Teter—Hutter pseudopotentials[27] that we employed, and the localized basis set of double-ζ plus polarization (DZVP) quality optimized to reduce the basis set superposition errors.[28] Calculations were performed using the Perdew—Burke—Ernzerhof (PBE) exchange correlation functional. Simulations were performed with nonperiodic boundary conditions in a 50 × 50 × 50 $Å^3$ unit cell for 2.5 nm quantum dot sizes. The quantum dot was carved out of bulk PbS. All singly bonded

atoms were discarded, resulting in a faceted cuboctahedron shape. A mixture of Cl and thiol ligands was used to passivate all dangling bonds on (111) and (110) facets, with the (100) facets left unpassivated. Care was taken to select the stoichiometry that preserves the charge neutrality of the dot, necessary to position the Fermi level in the midgap.[29] For all calculations, a single CQD was modeled with appropriate additions (MPA, deprotonated MPA, lead oleate as well as the monomer and dimer of the lead oleate—MPA complex). The lead oleate and complexes were not bound to the surface of the CQD but placed near the surface (approximately 3—5 Å). The distance was sufficient to observe no overlap between the electronic wave function of the states on the complex and those on the CQD itself.

REFERENCES AND NOTES

1. Steckel, J. S.; Coe-Sullivan, S.; Bulović, V.; Bawendi, M. G. 1.3 Mm to 1.55 Mm Tunable Electroluminescence from PbSe Quantum Dots Embedded within an Organic Device. *Adv. Mater.* **2003**, *15*, 1862–1866.

2. Qian, L.; Zheng, Y.; Xue, J.; Holloway, P. H. Stable and Efficient Quantum-Dot Light-Emitting Diodes Based on Solution-Processed Multilayer Structures. *Nat. Photonics* **2011**, *5*, 543–548.

3. Konstantatos, G.; Howard, I.; Fischer, A.; Hoogland, S.; Clifford, J.; Klem, E.; Levina, L.; Sargent, E. H. Ultrasensitive Solution-Cast Quantum Dot Photodetectors. *Nature* **2006**, *442*, 180–183.

4. McDonald, S. A.; Konstantatos, G.; Zhang, S.; Cyr, P. W.; Klem, E. J. D.; Levina, L.; Sargent, E. H. Solution-Processed PbS Quantum Dot Infrared Photodetectors and Photovoltaics. *Nat. Mater.* **2005**, *4*, 138–142.

5. Ip, A. H.; Thon, S. M.; Hoogland, S.; Voznyy, O.; Zhitomirsky, D.; Debnath, R.; Levina, L.; Rollny, L. R.; Carey, G. H.; Fischer, A.; *et al.* Hybrid Passivated Colloidal Quantum Dot Solids. *Nat. Nanotechnol.* **2012**, *7*, 577–582.

6. Murray, C. B.; Norris, D. J.; Bawendi, M. G. Synthesis and Characterization of Nearly Monodisperse CdE (E = Sulfur, Selenium, Tellurium) Semiconductor Nanocrystallites. *J. Am. Chem. Soc.* **1993**, *115*, 8706–8715.

7. Kramer, I. J.; Sargent, E. H. The Architecture of Colloidal Quantum Dot Solar Cells: Materials to Devices. *Chem. Rev.* **2014**, *114*, 863–882.

8. Wang, X.; Koleilat, G. I.; Tang, J.; Liu, H.; Kramer, I. J.; Debnath, R.; Brzozowski, L.; Barkhouse, D. A. R.; Levina, L.;

Hoogland, S.; *et al.* Tandem Colloidal Quantum Dot Solar Cells Employing a Graded Recombination Layer. *Nat. Photonics* **2011**, *5*, 480–484.

9. Semonin, O. E.; Luther, J. M.; Choi, S.; Chen, H.-Y.; Gao, J.; Nozik, A. J.; Beard, M. C. Peak External Photocurrent Quantum Efficiency Exceeding 100% *via* MEG in a Quantum Dot Solar Cell. *Science* **2011**, *334*, 1530–1533.

10. Chuang, C.-H. M.; Brown, P. R.; Bulović, V.; Bawendi, M. G. Improved Performance and Stability in Quantum Dot Solar Cells through Band Alignment Engineering. *Nat. Mater.* **2014**, *13*, 796–801.

11. Kirmani, A. R.; Carey, G. H.; Abdelsamie, M.; Yan, B.; Cha, D.; Rollny, L. R.; Cui, X.; Sargent, E. H.; Amassian, A. Effect of Solvent Environment on Colloidal-Quantum-Dot Solar-Cell Manufacturability and Performance. *Adv. Mater.* **2014**, *26*, 4717–4723.

12. Pan, J.; El-Ballouli, A. O.; Rollny, L.; Voznyy, O.; Burlakov, V. M.; Goriely, A.; Sargent, E. H.; Bakr, O. M. Automated Synthesis of Photovoltaic-Quality Colloidal Quantum Dots Using Separate Nucleation and Growth Stages. *ACS Nano* **2013**, *7*, 10158–10166.

13. Kramer, I.; Minor, J.; Moreno-Bautista, G.; Rollny, L.; Kanjanaboos, P.; Kopilovic, D.; Thon, S. M.; Carey, G. H.; Chou, K. W.; Zhitomirsky, D.; *et al.* Efficient Spray-Coated Colloidal Quantum Dot Solar Cells. *Adv. Mater.* **2014**, DOI: 10.1002/adma.201403281.

14. Kramer, I. J.; Moreno-Bautista, G.; Minor, J. C.; Kopilovic, D.; Sargent, E. H. Colloidal Quantum Dot Solar Cells on Curved and Flexible Substrates. *Appl. Phys. Lett.* **2014**, *105*, 163902.

15. *CRC Handbook of Chemistry and Physics Version 2010*; 90th ed.; Lide, D. R., Ed.; CRC Press: Boca Raton, 2010.

16. Ma, W.; Luther, J. M.; Zheng, H.; Wu, Y.; Alivisatos, A. P. Photovoltaic Devices Employing Ternary PbS_xSe_{1-X} Nanocrystals. *Nano Lett.* **2009**, *9*, 1699–1703.

17. Lingley, Z.; Lu, S.; Madhukar, A. A High Quantum Efficiency Preserving Approach to Ligand Exchange on Lead Sulfide Quantum Dots and Interdot Resonant Energy Transfer. *Nano Lett.* **2011**, *11*, 2887–2891.

18. Choi, J. J.; Luria, J.; Hyun, B.-R.; Bartnik, A. C.; Sun, L.; Lim, Y.-F.; Marohn, J. A.; Wise, F. W.; Hanrath, T. Photogenerated Exciton Dissociation in Highly Coupled Lead Salt Nanocrystal Assemblies. *Nano Lett.* **2010**, *10*, 1805–1811.

19. Voznyy, O.; Thon, S. M.; Ip, A. H.; Sargent, E. H. Dynamic Trap Formation and Elimination in Colloidal Quantum Dots. *J. Phys. Chem. Lett.* **2013**, *4*, 987–992.

20. Luther, J. M.; Law, M.; Song, Q.; Perkins, C. L.; Beard, M. C.; Nozik, A. J. Structural, Optical, and Electrical Properties of Self-Assembled Films of PbSe Nanocrystals Treated with 1,2-Ethanedithiol. *ACS Nano* **2008**, *2*, 271–280.

21. Fischer, A.; Rollny, L.; Pan, J.; Carey, G. H.; Thon, S. M.; Hoogland, S.; Voznyy, O.; Zhitomirsky, D.; Kim, J. Y.; Bakr, O. M.; *et al.* Directly Deposited Quantum Dot Solids Using a Colloidally Stable Nanoparticle Ink. *Adv. Mater.* **2013**, *25*, 5742–5749.

22. Hines, M. a.; Scholes, G. d. Colloidal PbS Nanocrystals with Size-Tunable Near-Infrared Emission: Observation of Post-Synthesis Self-Narrowing of the Particle Size Distribution. *Adv. Mater.* **2003**, *15*, 1844–1849.

23. Snaith, H. J. The Perils of Solar Cell Efficiency Measurements. *Nat. Photonics* **2012**, *6*, 337–340.

24. Kroon, J. M.; Wienk, M. M.; Verhees, W. J. H.; Hummelen, J. C. Accurate Efficiency Determination and Stability Studies of Conjugated Polymer/fullerene Solar Cells. *Thin Solid Films* **2002**, *403−404*, 223–228.

25. VandeVondele, J.; Krack, M.; Mohamed, F.; Parrinello, M.; Chassaing, T.; Hutter, J. Quickstep: Fast and Accurate Density Functional Calculations Using a Mixed Gaussian and Plane Waves Approach. *Comput. Phys. Commun.* **2005**, *167*, 103–128.

26. Lippert, G.; Hutter, J.; Parrinello, M. A Hybrid Gaussian and Plane Wave Density Functional Scheme. *Mol. Phys.* **1997**, *92*, 477–488.

27. Hartwigsen, C.; Goedecker, S.; Hutter, J. Relativistic Separable Dual-Space Gaussian Pseudopotentials from H to Rn. *Phys. Rev. B* **1998**, *58*, 3641–3662.

28. VandeVondele, J.; Hutter, J. Gaussian Basis Sets for Accurate Calculations on Molecular Systems in Gas and Condensed Phases. *J. Chem. Phys.* **2007**, *127*, 114105.

29. Voznyy, O.; Zhitomirsky, D.; Stadler, P.; Ning, Z.; Hoogland, S.; Sargent, E. H. A Charge-Orbital Balance Picture of Doping in Colloidal Quantum Dot Solids. *ACS Nano* **2012**, *6*, 8448–8455.